Is Earendel a Star Cluster?: Metal-poor Globular Cluster Progenitors at $z \sim 6$

Massimo Pascale[1] , Liang Dai[2] , Brenda L. Frye[3] , and Aliza G. Beverage[1]

[1] Department of Astronomy, University of California, 501 Campbell Hall #3411, Berkeley, CA 94720, USA
[2] Department of Physics, University of California, 366 Physics North MC 7300, Berkeley, CA 94720, USA
[3] Department of Astronomy/Steward Observatory, University of Arizona, 933 N. Cherry Avenue, Tucson, AZ 85721, USA

Abstract

The strongly lensed $z \sim 6$ Sunrise galaxy offers an incredible opportunity to investigate star formation in the early Universe on parsec or smaller scales. The highly magnified object Earendel within the Sunrise was previously identified as a candidate star or binary owing to size constraints placed by the lensing magnification; however, recent works have suggested that this constraint may be relaxed to even the size of star clusters. Here we explore the hypothesis that Earendel may actually be a star cluster, and we simultaneously evaluate other star clusters within the host galaxy. Leveraging deep, archival James Webb Space Telescope NIRSpec PRISM spectroscopy, we determine a spectroscopic redshift for the Sunrise galaxy $z = 5.926 \pm 0.013$, and we fit simple stellar population (SSP) models from three premier libraries to evaluate the physical parameters of Earendel and another distinct star cluster in the Sunrise dubbed "1b." We find the rest-UV through optical continuum of Earendel to be well described by an SSP, nearly equivalently to 1b, which is confidently a star cluster. We infer that they have intermediate ages $t_{\mathrm{age}} \sim 30$–150 Myr, are metal-poor ($Z_\star \lesssim 0.1\,Z_\odot$), and are consistent with the formation age–metallicity trend seen in local globular clusters. Such intermediate-age clusters are seldom probed spectroscopically in the high-redshift Universe, and we explore the extent to which these clusters can be characterized via the spectroscopic continuum.

1. Introduction

Strong gravitational lensing has enabled the study of distant galaxies at unprecedented spatial scales (e.g., E. Vanzella et al. 2017; L. Mowla et al. 2022). High magnification from foreground galaxy clusters stretches background galaxies, resolving individual stellar associations such as parsec-scale star clusters at a high signal-to-noise ratio (SNR; M. Pascale et al. 2023; E. Vanzella et al. 2023). While strong-lensing magnification is typically on the order of dozens or fewer, compact stellar sources serendipitously situated near the lensing caustic can be magnified by factors of hundreds to thousands (e.g., B. Welch et al. 2022b; M. Pascale & L. Dai 2024). In extreme cases, even individual stars may be detectable in sensitive space-based imaging (J. Miralda-Escudé 1991; L. Dai et al. 2018; R. A. Windhorst et al. 2018; J. M. Diego 2019). These have been observed in low-to-intermediate-redshift ($z \lesssim 1$) galaxies strongly lensed by a foreground galaxy cluster (e.g., P. L. Kelly et al. 2018; S. A. Rodney et al. 2018; W. Chen et al. 2019; A. A. Kaurov et al. 2019; M. Pascale et al. 2022; Y. Fudamoto et al. 2025), assisted by temporary flux boosts induced by microlensing from intracluster stars (T. Venumadhav et al. 2017; J. M. Diego et al. 2018; M. Oguri et al. 2018; L. Weisenbach et al. 2024).

In other cases, it is thought that the source-caustic alignment can be so fortuitous that strong lensing alone delivers sufficiently large magnification factors ($\sim 10^4$) to reveal individual stars in high-redshift galaxies ($z \gtrsim 5$) in deep

Hubble Space Telescope (HST) or James Webb Space Telescope (JWST) imaging (e.g., J. M. Diego et al. 2023; A. K. Meena et al. 2023; L. J. Furtak et al. 2024). The first such example reported is Earendel (B. Welch et al. 2022a, 2022b) at $z \sim 6$, which remains the highest-redshift lensed star candidate identified to date. Earendel, or WHL 0137-LS, was discovered in the WHL J013719.8−82841 galaxy cluster field in HST imaging acquired through the RELICS program (D. Coe et al. 2019; B. Salmon et al. 2020). The HST discovery was first presented in B. Welch et al. (2022b) and later with JWST NIRCam imaging in B. Welch et al. (2022a). Earendel is thought to be persistently magnified by factors of 10^3–10^4, due to a close proximity to the lensing critical curve and the fact that the image flux appears stable across a 2 yr baseline in the observer frame, indicating that its brightness is not primarily a result of microlensing.

Synthesizing the predictions of four strong-lensing models of the foreground galaxy cluster ($z_{\mathrm{cluster}} = 0.566$), B. Welch et al. (2022a) constrain the intrinsic size of Earendel to be $r \lesssim 0.02$ pc, or ~ 4000 au, placing it at the scale of an individual stellar system rather than a star cluster. B. Welch et al. (2022a) found that JWST NIRCam photometry is not well fit by a single star, but rather that a binary system of two $\sim 20\,M_\odot$ stars of effective temperatures $\sim 34,000$ and 9000 K is more consistent with the data. Given the tight size constraint provided by strong-lensing models, a simple stellar population (SSP) fit has not been explored in that work or other prior works on Earendel.

L. Ji & L. Dai (2025) recently identified that in cases such as Earendel deriving size constraints solely from macro strong-lensing models can be prone to bias, as such models only include dark matter subhalos that have galaxies visible in HST or JWST imaging. In the hierarchical picture of structure

formation in ΛCDM cosmology, the dark matter subhalo population likely extends below the typical galactic mass scale ($\sim 10^{10}\ M_\odot$) down to $10^6\ M_\odot$ or even smaller. Such small subhalos are optically invisible but can have a pronounced effect on the lensing caustic strength while only modestly affecting the deflection and hence astrometric position of the lensed object (L. Dai et al. 2018, 2020; L. L. R. Williams et al. 2024). Indeed, L. Ji & L. Dai (2025) find through a combination of semianalytic modeling and numerical ray-tracing that accounting for this population of subhalos relaxes the constraint on the source size on the visible side of the caustic derived in B. Welch et al. (2022a) to as large as ~ 3 pc without contradicting observations. This light-weighted size is compatible with many of the massive star clusters seen both in the local Universe (for a review see M. R. Krumholz et al. 2019) and at high redshift (e.g., A. Adamo et al. 2024) and has reopened the discussion on the nature of Earendel and other similar highly magnified high-redshift sources.

Recently, Z. P. Scofield et al. (2025) have also shown from a macroscopic analysis (i.e., not including the subhalos treat-ment of L. Ji & L. Dai 2025) that Earendel's magnification may be as low as $\mu \sim 50$. While L. Ji & L. Dai (2025) assume the strong-lensing models of B. Welch et al. (2022b) that predict magnifications in excess of 1000 and then subsequently evaluate how this changes in the presence of dark matter subhalos, Z. P. Scofield et al. (2025) construct a new joint strong- and weak-lensing model, which itself finds that Earendel may only be modestly magnified. The approach of Z. P. Scofield et al. (2025) was found to accurately predict magnifications for SN H0pe, the only multiply imaged source in the galaxy cluster lensing regime with a known magnifica-tion in the literature (B. L. Frye et al. 2024; M. Pascale et al. 2025), and further draws the nature of Earendel into question.

Motivated by the conclusions of L. Ji & L. Dai (2025) and Z. P. Scofield et al. (2025), in this Letter we consider whether Earendel could instead be a compact star cluster rather than an individual star or star system, and we simultaneously evaluate other stellar knots within the Sunrise galaxy. Sunrise is known to host multiple compact star clusters with exceptional stellar surface densities ($>10^4\ M_\odot\,\mathrm{pc}^{-2}$) at both young ($<10$ Myr) and evolved ages (E. Vanzella et al. 2023). More generally, strongly lensed galaxies have revealed an abundance of high-density star clusters, which are rare in our cosmic backyard (e.g., A. Adamo et al. 2024; S. Fujimoto et al. 2024; M. Messa et al. 2025; K. E. Whitaker et al. 2025). These clusters can probe vigorous star formation, which may be more common-place in the high-redshift Universe, and furthermore may be the progenitors of locally observed globular clusters (GCs) whose origin and evolution are not yet fully understood (e.g., E. Vanzella et al. 2017). Deep UV−optical spectroscopic studies of these clusters are sparse, particularly for evolved cluster ages >10 Myr. At the redshift of Sunrise, deep, publicly available NIRSpec spectroscopy covers the rest-UV through optical of Earendel, as well as multiple other stellar clumps within the galaxy that are more widely accepted as star clusters. Hence, Earendel and the Sunrise galaxy may be valuable assets for furthering our understanding of high-redshift star clusters.

In Section 2, we describe the data sets used for this analysis, including archival JWST NIRSpec spectroscopy, which has not been evaluated in prior literature on the Sunrise galaxy. Section 3 details the methods involved, including derivation of

the spectroscopic redshift and the spectral energy distribution (SED) fitting to derive the physical properties. We discuss the results and the nature of Earendel, as well as other stellar clumps in the Sunrise galaxy, in Section 4. We evaluate whether the spectrum is consistent with the expectation of a star cluster, and we assess how this system relates to the picture of star cluster formation and evolution. In Section 5, we provide concluding remarks on this analysis.

2. Observations

This work makes use of JWST data sets that are available on the MAST archive. JWST NIRCam imaging is not directly used in this analysis; however, photometry results from B. Welch et al. (2022a) and E. Vanzella et al. (2023) that make use of images from Cycle 1 Go program 2282 (PI: Coe) are used. JWST NIRSpec PRISM spectra were queried from version 3 of the DAWN JWST Archive (DJA; K. E. Heintz et al. 2024), which makes use of `msaexp` (G. Brammer 2022) for the reduction pipeline; further details can be found in K. E. Heintz et al. (2024) and A. de Graaff et al. (2025). We highlight that the background subtraction is performed using a "master sky background" approach that fits to empty portions of the source slitlets and optimizes for SNR as described in Appendix A of A. de Graaff et al. (2025). We make use of four spectra in the Sunrise for Earendel, image 1b, image 1a, and one of the star-forming regions along the Sunrise arc, which correspond to 2282_10000, 2282_10002, 2282_10001, and 2282_12001, respectively. The Sunrise galaxy and clumps of interest are shown in Figure 1. The Earendel and 1b spectra are shown in Figure 2. We note that the singular emission-line spectrum, 2282_1200, may contain a combination of images 4, 5, and 6, which are denoted in E. Vanzella et al. (2023) as making up a so-called "star-forming complex" (SFC). This spectrum is only used for the spectroscopic redshift measure-ment, and as such the multicomponent aspect of this spectrum is not accounted for in this work.

We adopt the nomenclature of E. Vanzella et al. (2023) for image system designations in this work (see our Figure 1 or their Figure 2). However, we note that the system of d images of the SFC is somewhat misleading, as these images have an opposite parity to the system of b images, indicating that there must be an odd number of critical curve crossings through the Sunrise arc between the b and d systems. Z. P. Scofield et al. (2025) similarly point out that the image system designations may be inaccurate. For simplicity, we retain the nomenclature used in previous works; however, we caution that the image system designations are subject to change in future works.

3. Methods

3.1. Redshift Determination

We determine the spectroscopic redshift of the Sunrise arc via nebular line emission detected in slit 12282_12001, which contains SFCb on the arc (see Figure 1) consisting of *4b, 5b,* and *6b* (see nomenclature in E. Vanzella et al. 2023). The spectrum shows clear detections of [O II] $\lambda\lambda3727$, 3729, [Ne III] $\lambda3869$, Hβ, [O III] $\lambda\lambda4959$, 5007, and Hα at SNR $\gtrsim 5$. The redshift is determined via simultaneous fitting of Gaussian line profiles to the H-Balmer and [O III] features, yielding $z = 5.926^{+0.013}_{-0.012}$. This is consistent with the Lyman-series break spectroscopically observed in the stellar continuum of other knots within the Sunrise (e.g., Earendel, $1a/b$). Our
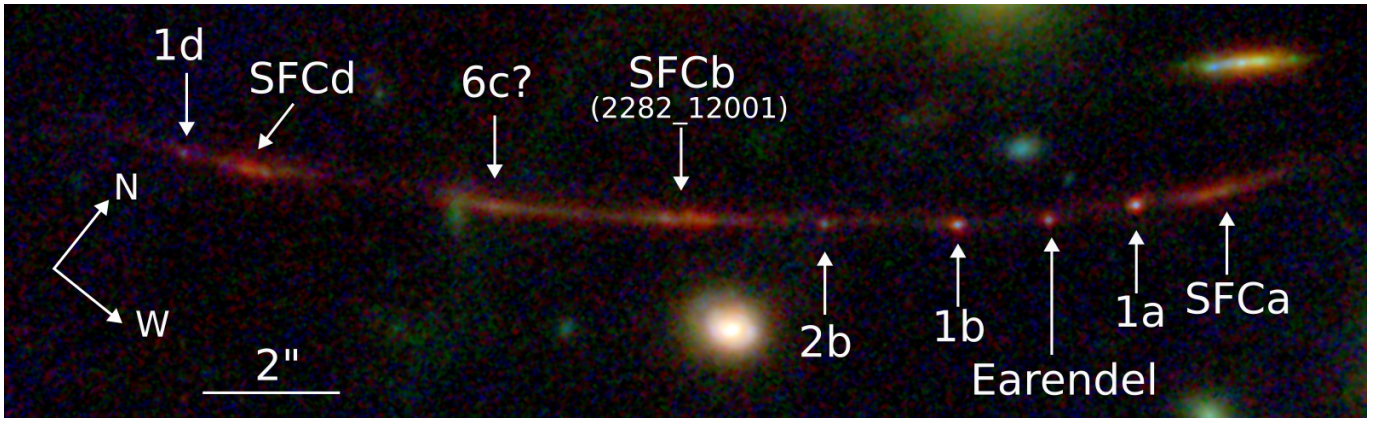
Figure 1. JWST NIRCam F090W+F200W+F444W false-color image of the Sunrise galaxy at $z \approx 5.93$. The multiple images shown sweep out an angular extent of $\sim 16''$. At the redshift of Sunrise, the compass $2''$ corresponds to ~ 11.8 kpc. Labeled are multiply imaged clumps of interest within the galaxy: Earendel, image 1, image 6, and the SFC, consisting of images 3, 4, 5, and 6. We note the JWST NIRSpec MSA slit ID that covers image b of the SFC, 2282_12001, which is used for the spectroscopic redshift measurement.

spectroscopic measurement is lower than the photometric redshift $z_{\rm phot} = 6.2 \pm 0.1$ inferred by B. Welch et al. (2022a) but consistent with the $z_{\rm phot} = 5.9^{+0.3}_{-0.2}$ determined by E. Vanzella et al. (2023).

3.2. SED Fitting

We perform SED fitting to the continuum of Earendel and the lensed knot 1b to infer their physical parameters. We also perform fitting to the counterimage of 1b, 1a, whose spectrum has lower SNR but is useful for testing the robustness of the fitting procedure, as 1b and 1a should ideally yield comparable results. We choose to fit only to the NIRSpec spectrum rather than performing a joint photometric−spectroscopic fit. B. Welch et al. (2022a) performed detailed photometry of Earendel synthesizing 14 different measurements conducted by 10 separate people (a so-called "wisdom of crowds" approach); however, we find the B. Welch et al. (2022a) measurements to disagree with the spectroscopic continuum at the $\gtrsim 20\%$ level in Earendel, and the F115W filter flux measurement features an enhancement that is not seen in the spectrum (see Figure 6 of B. Welch et al. 2022a). Given the thoroughness of the B. Welch et al. (2022a) approach, we speculate that systematics may dominate the photometric error, or that the F115W filter may suffer from an artifact at the location of Earendel.

This photometric−spectroscopic tension is not seen in the neighboring knot, 1b; however, as a caution we opt to fit only to the NIRSpec spectrum in all cases. While systematics from the spectroscopic calibration may affect the results, we find that the goodness of fit is reasonable in all spectroscopic fits and furthermore that including photometry with the F115W filter removed generally agrees to within 1σ. Stellar masses are measured by scaling to the F200W filter photometry from B. Welch et al. (2022a) and E. Vanzella et al. (2023), with the exception of 1a, which does not have existing photometry in the literature and is only used to probe systematics in the SED fitting.

SED fitting is conducted by fitting an SSP to the observed NIRSpec spectra. The approach is modeled after the well-tested Bagpipes software (A. C. Carnall et al. 2018, 2019); however, our methodology is optimized for use of instantaneous burst star formation histories (SFHs), which is likely appropriate for an individual star cluster (A. Wofford et al.

2016). We briefly describe the approach below, noting that the methodology follows Bagpipes unless specified otherwise. We also test an exponentially decaying SFH in Appendix A.

The stellar SED is constructed using three separate well-known SSP libraries to account for systematics involving the SSP used: (1) BPASS (E. R. Stanway et al. 2016) including binary evolution and using an initial mass function (IMF) $\xi(m) \propto m^{-1.3}$ for $m < 0.5\,M_\odot$ and $\xi(m) \propto m^{-2.35}$ for $m > 0.5\,M_\odot$ in the initial stellar mass range $0.1 < m/M_\odot < 100$, (2) the 2016 version of the BC03 (G. Bruzual & S. Charlot 2003; J. Chevallard & S. Charlot 2016) models using a P. Kroupa (2001) IMF and an upper-mass cutoff $M_{\rm cut} = 100\,M_\odot$, and (3) FSPS (C. Conroy & J. E. Gunn 2010) using the MIST (J. Choi et al. 2016) isochrones with the MILES empirical stellar library and a P. Kroupa (2001) IMF with an upper-mass cutoff $M_{\rm cut} = 120\,M_\odot$.

For each SSP library, we construct a grid of ages and metallicities using values natively available from the library that we linearly interpolate across in $\log(t_{\rm age})$ and metallicity to yield the stellar SED. This is the primary difference between our approach and Bagpipes, which resamples the SSP age grid using a weighted summation approach (A. C. Carnall et al. 2018). In fitting, the population age is allowed to vary freely from 1 Myr to 1 Gyr (roughly the age of the Universe at this redshift), and the metallicity is optimized in the range $Z/Z_\odot \in (0.0005, 1)$ for BPASS and $Z/Z_\odot \in (0.005, 1)$ for BC03 and FSPS (where $Z_\odot = 0.0142$; M. Asplund et al. 2021).

We also include a nebular component with free ionization parameter $\log U \in (-4, -1)$ and free covering factor $x \in (0, 1)$, which directly scales the nebular component flux. The nebular component is constructed using CLOUDY (G. J. Ferland et al. 2017) with input incident radiation from the stellar SEDs that make up our grid. For each nebular realization, we fix the gas-phase metallicity to the metallicity of the input stellar population, assume rescaled solar chemical abundances (with the exception of He and N, which follow M. A. Dopita et al. 2000), and use a fixed electron density $n_e = 100\,{\rm cm}^{-2}$. Unlike BAGPIPES, we extend the nebular grid to include stellar populations out to 1 Gyr, as stripped stars may provide a nonnegligible ionizing budget through the first ~ 100 Myr of the cluster lifetime (Y. Götberg et al. 2019).

We note that we identify candidate marginal detections of [O III] $\lambda 5007$ and Hα in the Earendel spectrum, which are
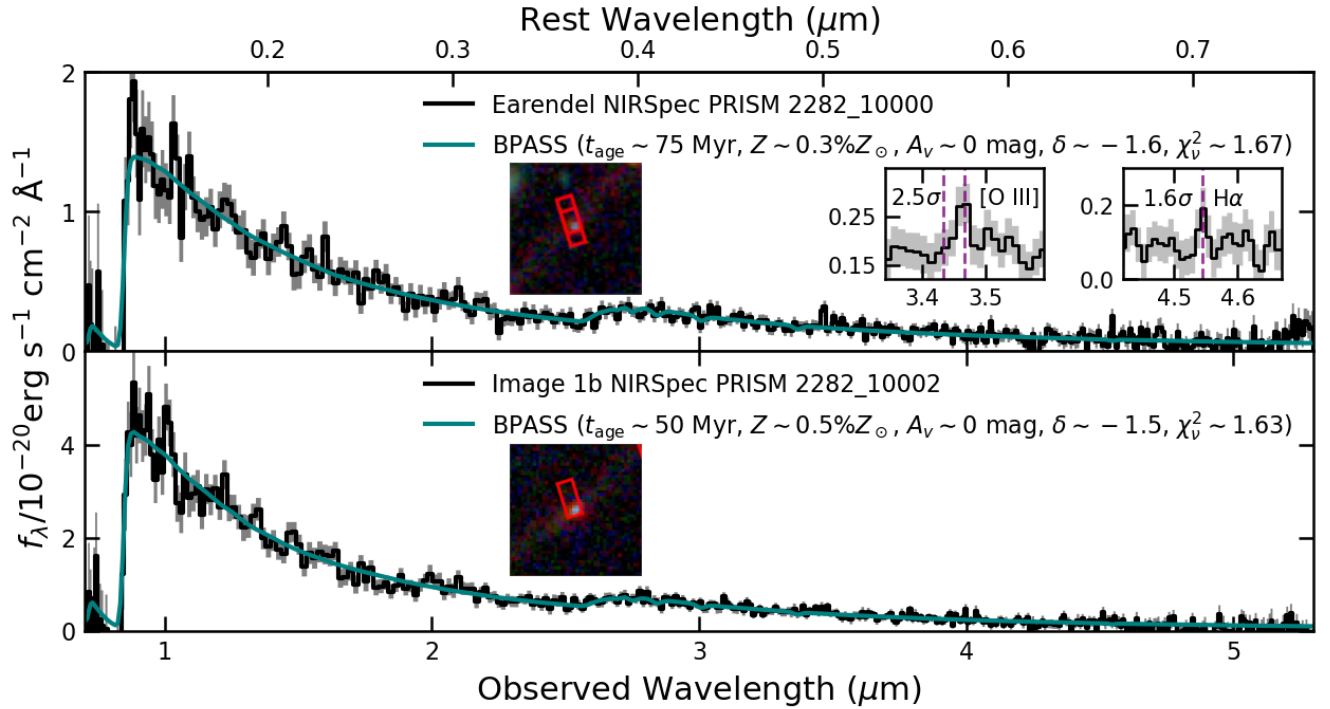
Figure 2. NIRSpec PRISM spectra of Earendel and 1*b* with the best-fit `BPASS` model from SED fitting overplotted. We omit the BC03 and `FSPS` best-fit SEDs for clarity, as they appear similar to the result from `BPASS`. Spectra are taken from version 3 of the DJA (K. E. Heintz et al. 2024). Both Earendel and 1*b* have similar spectra indicative of stellar continuum from an evolved SSP. The fit is influenced by the shape of the continuum, the lack of significant absorption features, and the clear Balmer break seen in both spectra. SED fitting measures similar parameters for these two objects, which are labeled approximately. Left insets show stamps from a JWST false-color image with the NIRSpec MSA slits overplotted. Right insets show smoothed zoom-ins of the Earendel spectrum where we identify marginal detections of nebular line emission [O III] $\lambda5007$ ([O III] $\lambda4959$ nondetection also marked) and Hα, which are measured at 2.5σ and 1.6σ significance, respectively.

measured to 2.5σ and 1.6σ significance, respectively. Investigation of the 2D spectrum shows that these features appear only marginally more extended than the underlying continuum, and we cannot rule out that they result from contamination from the arc background. As a caution we masked these features, but note that their inclusion was not found to impact the posterior of the fits.

We apply an interstellar medium (ISM) dust reddening law following S. Salim et al. (2018), which includes a free reddening power-law slope on which we force a prior $\delta \in [-2.0, 0.75]$. This has the freedom to reproduce both the D. Calzetti (2001) ($\delta = 0$) and SMC ($\delta \sim -0.45$) reddening curves, as well as significantly steeper curves $\delta < -1$, which may be better representative of low-mass, high-redshift galaxies (S. Salim et al. 2018). We also include a free 2175 Å bump strength $B \in [0, 3]$ where $B = 3$ matches the Milky Way (MW) bump strength of J. A. Cardelli et al. (1989). Intergalactic medium attenuation and dust emission follow exactly the prescription of `Bagpipes`, and we refer the reader to A. C. Carnall et al. (2018) for further details.

The system redshift was allowed to vary following a Gaussian prior with median and width $(\mu, \sigma) = (5.926, 0.013)$ following the redshift determined in Section 3.1. The spectral resolution was set by the NIRSpec PRISM resolution curves provided by the JWST User documentation (JDox)[4]—as Earendel and image 1 are point-like sources, their position in the slit may affect the wavelength-dependent spectral resolution (A. de Graaff et al. 2024); however, the resolution curve provided by JDox is likely a sufficient approximation for this

analysis. We additionally allow for a velocity dispersion $\sigma \in (1, 100)\,\mathrm{km\,s^{-1}}$, encompassing the range of dispersions seen in even the most compact star clusters. Finally, we include an additional white-noise scaling term $\alpha \in (1, 10)$, which directly scales the NIRSpec spectrum uncertainties and can help mitigate both underestimation of uncertainties and SED model systematics.

The resulting model consists of 10 free parameters for 407 observables with 397 degrees of freedom. Parameter inference is computed using `Nautilus` (J. U. Lange 2023) using 3000 live points. Robustness of the posterior is ensured following recommendations from J. U. Lange (2023), specifically that (1) increasing the number of live points does not change the result, (2) points from the exploration phase are discarded, and (3) the shell-bound occupation fraction is unity beyond the earliest iterations.

We perform two primary tests to address underestimation of uncertainties beyond the inclusion of the white-noise scaling term. We first test whether outlier features, such as those at ~ 10500 Å observer frame in the Earendel spectrum (see Figure 2), skew the fit by masking them, which we did not find to meaningfully impact the posteriors. We also test in the limiting case where the intrinsic spectrum is mostly smooth, by applying a boxcar smoothing function from the spectrum redward of the Lyman-series limit. We subtract the smoothed spectrum from the original, which was found to approximately center at zero, and then calculate a running standard deviation across the spectrum. We find this running standard deviation to be consistent with the uncertainties applied in fitting after accounting for the best-fit white-noise scaling. Furthermore, recomputing the fit assigning the running standard deviation as

---

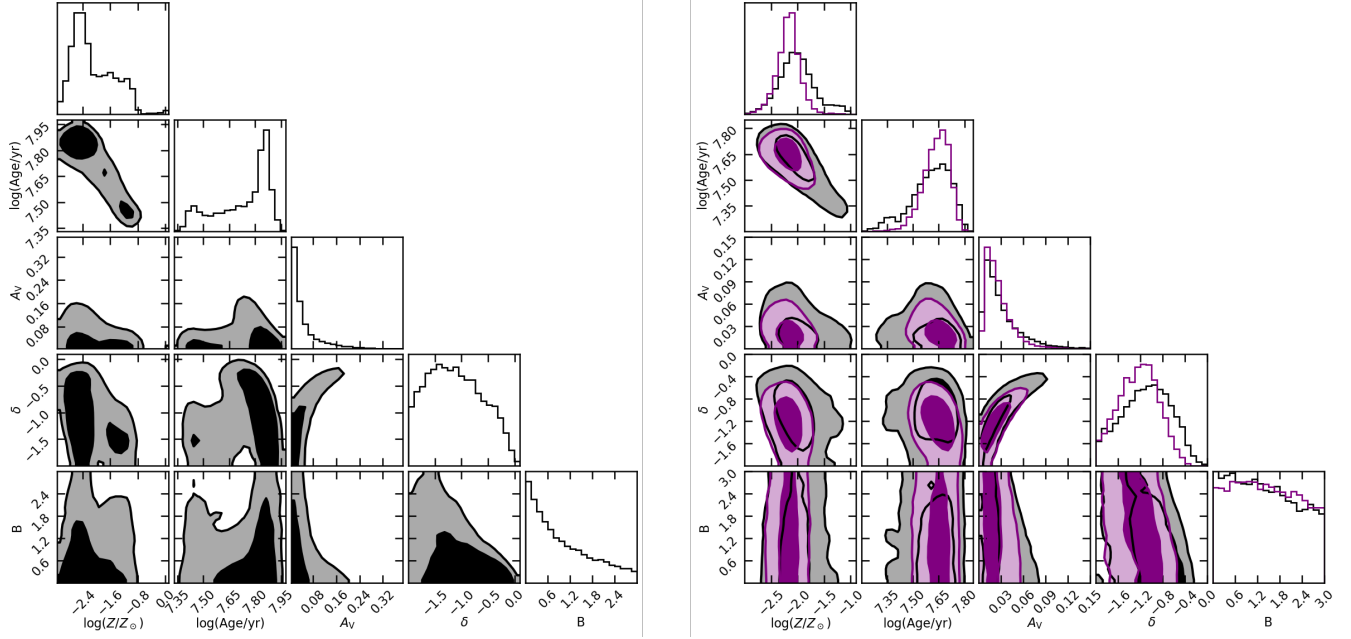[4] JWST NIRSpec PRISM Resolution Curve

Figure 3. Posterior distributions for the Earendel (left), 1*b* (right purple), and 1*a* (right black) physical parameters from fitting with the BPASS SSP library, which generally yielded the largest age and metallicity uncertainties. We omit the ionization parameter, covering factor, and velocity dispersion, as they go unconstrained. We also omit the white-noise scaling, which is $\lesssim 1.3$ in all cases. 2D contours enclose 50% and 90% of the posterior samples. Refer to Table 1 for the 68% confidence intervals of the parameters.

Table 1
SED Parameters

Image	SSP	$\log(t_{age}/\mathrm{yr})$	$\log(\mu M/M_\odot)$	$\log(Z/Z_\odot)$	A_V (mag)	δ	B	χ^2_ν
Earendel	BC03	$7.50^{+0.04}_{-0.04}$	$8.87^{+0.03}_{-0.04}$	$-1.67^{+0.26}_{-0.21}$	$0.03^{+0.03}_{-0.01}$	$-1.44^{+0.44}_{-0.35}$	$0.98^{+1.10}_{-0.71}$	1.71
	BPASS	$7.79^{+0.08}_{-0.27}$	$9.06^{+0.07}_{-0.23}$	$-2.28^{+0.90}_{-0.38}$	$0.03^{+0.06}_{-0.02}$	$-1.15^{+0.61}_{-0.52}$	$0.77^{+1.17}_{-0.59}$	1.67
	FSPS	$8.05^{+0.14}_{-0.27}$	$9.24^{+0.18}_{-0.23}$	$-1.67^{+0.48}_{-0.40}$	$0.05^{+0.14}_{-0.04}$	$-0.09^{+0.49}_{-0.93}$	$0.73^{+1.19}_{-0.56}$	1.68
Im 1*b*	BC03	$7.47^{+0.01}_{-0.02}$	$9.21^{+0.02}_{-0.02}$	$-2.12^{+0.05}_{-0.03}$	$0.03^{+0.02}_{-0.01}$	$-1.25^{+0.29}_{-0.30}$	$1.57^{+0.94}_{-0.97}$	1.65
	BPASS	$7.64^{+0.06}_{-0.08}$	$9.33^{+0.04}_{-0.06}$	$-2.17^{+0.18}_{-0.21}$	$0.02^{+0.02}_{-0.01}$	$-1.22^{+0.34}_{-0.39}$	$1.40^{+1.02}_{-0.93}$	1.63
	FSPS	$8.21^{+0.03}_{-0.05}$	$9.73^{+0.05}_{-0.05}$	$-2.41^{+0.12}_{-0.06}$	$0.02^{+0.05}_{-0.02}$	$0.30^{+0.33}_{-0.61}$	$1.42^{+1.03}_{-0.97}$	1.65
Im 1*a*	BC03	$7.47^{+0.02}_{-0.02}$	[a]$9.07^{+0.02}_{-0.01}$	$-2.10^{+0.07}_{-0.04}$	$0.03^{+0.02}_{-0.01}$	$-1.29^{+0.33}_{-0.35}$	$1.49^{+0.97}_{-0.96}$	1.77
	BPASS	$7.62^{+0.10}_{-0.13}$	[a]$9.17^{+0.08}_{-0.11}$	$-2.03^{+0.33}_{-0.31}$	$0.02^{+0.03}_{-0.01}$	$-1.08^{+0.43}_{-0.48}$	$1.32^{+1.08}_{-0.92}$	1.72
	FSPS	$8.01^{+0.11}_{-0.13}$	[a]$9.42^{+0.14}_{-0.11}$	$-1.81^{+0.33}_{-0.40}$	$0.04^{+0.07}_{-0.03}$	$0.30^{+0.32}_{-0.51}$	$1.26^{+1.13}_{-0.90}$	1.77

Notes. Physical parameters for Earendel, image 1*b*, and image 1*a* of the Sunrise arc using three separate SSP libraries: the 2016 version of the G. Bruzual & S. Charlot (2003; BC03) models (J. Chevallard & S. Charlot 2016), BPASS (E. R. Stanway et al. 2016), and FSPS (C. Conroy & J. E. Gunn 2010). We list the object, the SSP library, the burst age, the magnified stellar mass (μ is the flux magnification factor due to lensing), the stellar metallicity, visual band extinction, reddening law slope following S. Salim et al. (2018), reddening law 2175 Å bump strength following S. Salim et al. (2018), and the reduced χ^2 statistic for 397 degrees of freedom without the ~30% white-noise scaling applied. While the nebular ionization parameter and covering factor are also optimized for in this analysis, they are omitted from the table for clarity, as they go unconstrained within their uniform priors listed in Section 3.
[a] The 1*a* magnified mass is derived solely from the spectrum and not via rescaling to the measured F200W flux, as is the case for Earendel and 1*b*. The 1*a* spectrum suffers from slit loss, and the mass is likely underestimated by a factor of 2–3.

the error was found to produce similar results to the assigned errors.

4. Results and Discussion

4.1. Metal-poor Globular Cluster Progenitors

We find the Earendel spectrum to be highly consistent with that of an SSP across all three SSP libraries. Each library produces a comparable best fit, in each case requiring a white-noise scaling ~1.3 to reach a reduced χ^2 of unity, translating to a typical $\chi^2_\nu \sim 1.7$ without the noise scaling term. We similarly see a nearly equivalent goodness of fit for image 1*b*,

which is commonly accepted to be a star cluster. We reassuringly find that repeating the same fitting procedure for the 1*a* spectrum yields comparable results to 1*b*, as seen in Figure 3 and Table 1. The results of BPASS and BC03 strongly agree to within 1σ, while the FSPS fits show a weaker $\sim 2\sigma$ level agreement but remain qualitatively similar.

The best-fit spectrum from the BPASS templates is shown in Figure 2. All three SSP libraries produce qualitatively similar posteriors for both Earendel and 1*b*; however, some physical parameters disagree to $\gtrsim 2\sigma$. The inferred parameters are given in Table 1, and the BPASS posteriors are plotted in Figure 3. For both Earendel and 1*b*, we infer an evolved (>30 Myr),

metal-poor ($Z/Z_\odot < 10\%$) star cluster with a magnified mass $\mu M \sim 10^9\, M_\odot$ and a minimal ISM dust reddening $A_V < 0.1$ mag. We do not find the velocity dispersion to be well constrained, nor does it significantly impact the posteriors, reflecting both the low spectral resolution of PRISM and the lack of significant absorption features.

4.1.1. Stellar Surface Density

The Sunrise galaxy is well-known to host some of the highest stellar surface density clusters observed, and indeed E. Vanzella et al. (2023) determine from photometrically derived stellar masses and astrometrically derived sizes the stellar surface density of 1b to be $\Sigma_\star \approx 3 \times 10^5(\frac{\mu}{70})\, M_\odot\, \mathrm{pc}^{-2}$. We find that our updated spectroscopically derived stellar masses are higher than those determined by E. Vanzella et al. (2023), a consequence of generally older derived ages. Assuming the magnification and size estimates of E. Vanzella et al. (2023) and our BPASS results (the intermediate of the three SSP mass estimates) of $M_\star/M_\odot \approx 2.5 \times 10^7(\frac{\mu}{70})$, we estimate the 1b stellar surface density to be $\Sigma_{\star,1b} \approx 1.3 \times 10^6(\frac{\mu}{70})\, M_\odot\, \mathrm{pc}^{-2}$.

The stellar surface density measurement for Earendel is less straightforward, as the magnification and size measurements are not well understood. B. Welch et al. (2022a) find the apparent surface brightness of Earendel to be approximately consistent with the point-spread function in JWST NIRCam F090W imaging, placing the apparent source size below the that of a native JWST pixel ($0\overset{''}{.}031 \sim 200$ pc at $z = 5.926$).

In the simulations of L. Ji & L. Dai (2025), the light of Earendel is dominated by a single lensed image, and the intrinsic source size may be as large as 1–3 pc while still appearing below this $0\overset{''}{.}031$ limit. Additionally, new strong-lensing models by Z. P. Scofield et al. (2025) find macroscopically (e.g., without subhalos) that Earendel's magnification may be as low as $\mu \sim 40$–70, further complicating the choice of magnification.

We consider a range of fiducial tangential magnifications $\mu_t \sim 50$–500 with an assumed radial magnification $\mu_r \sim 2$, producing far-ultraviolet (FUV) size upper limits $r_{\mathrm{FUV}} \approx 0.4$–4 pc and star clusters of masses $M_\star/M_\odot \approx 10^6 - 10^7$ assuming the BPASS posterior median. The resulting stellar surface density upper limit is hence $\Sigma_{\star,e} \approx 3 \times 10^5 - 10^6\, M_\odot\, \mathrm{pc}^{-2}$.

Both Earendel and 1b produce incredible stellar surface densities, which for some magnifications exceed the observed $\Sigma_{\star,\mathrm{max}} \approx 3 \times 10^5\, M_\odot\, \mathrm{pc}^{-2}$ ceiling seen in local Universe clusters (P. F. Hopkins et al. 2010; M. Y. Grudić et al. 2019). Such densities may indicate that the star formation in these clusters is feedback free, allowing for higher star formation efficiency and hence higher stellar densities (A. Dekel et al. 2023). However, C. E. Williams et al. (2025) determine that in such a scenario clusters of stellar surface density $\log(\Sigma_\star) > 10^5$ and $M_\star > 10^6\, M_\odot$ are typically bound yet nonvirialized; such high densities may not be maintained across the cluster evolution to the present day. Highly efficient star formation may also be conducive for the formation of populations with top-heavy IMFs (e.g., S. H. Menon et al. 2024; W. Lake et al. 2025); however, we did not find that implementing SSPs with a top-heavy IMF ($\xi(m) \propto m^{-2.00}$ for $m > 0.5\, M_\odot$) meaningfully changed the stellar mass estimates. Finally, we note that we derive these

stellar surface densities using rest-FUV sizes, which, due to mass segregation (e.g., M. W. Hosek et al. 2015; U. Mestric et al. 2023), may be smaller than the optical sizes typically quoted for local Universe clusters or those quoted from simulations.

4.1.2. Age and Metallicity

All three SSPs show general agreement at the $\sim 1\sigma$ level in their metallicity predictions for both Earendel and 1b and consistently predict the metallicity to be in the metal-poor regime. Choosing whichever SSP posterior predicts the highest metallicities (generally BPASS), the inferred posteriors rule out $Z/Z_\odot > 10\%$ to $\sim 95\%$ confidence in Earendel and $\sim 99\%$ confidence for 1b. Similarly $Z/Z_\odot > 5\%$ is ruled out to $\sim 80\%$ and $\sim 99\%$ confidence for Earendel and 1b, respectively. We point out that the uncertainties quoted for the BPASS fit of Earendel are somewhat misleading. Figure 3 reveals that the age–metallicity posterior is closer to double-peaked rather than classically broad, and metal-poor solutions are strongly favored.

We found that these metallicity measurements were influenced primarily by the shape of the spectroscopic continuum (e.g., the UV and optical slopes, the observed Balmer break), as the depth of absorption features was not found to approach the flux uncertainties until $Z \sim 0.5\, Z_\odot$. While we are cautious to assign an exact metallicity to either Earendel or 1b given the potential systematics, the synthesis of the three SSP fits confidently places these clusters in the metal-poor regime ($\lesssim 10\%\, Z_\odot$). Further tests assessing systematics in the metallicity measurement are detailed in Appendix B.

The ages are in weaker agreement with one another compared to the metallicity. For Earendel the SSPs predict a wide range of ages 30–110 Myr, and the uncertainties are of order tens of Myr. In the case of 1b the statistical precision is much higher (noting that uncertainties are scaled up $\sim 30\%$ via a white-noise term), with BC03, BPASS, and FSPS predicting $t_{\mathrm{age}} \sim 30$, 45, and 160 Myr, respectively, to within a $\sim$few Myr precision. This may be reflective of the overall slow evolution of the stellar continuum beyond 10 Myr and perhaps somewhat poorly understood ingredients in the SSP such as the treatment of binaries (though we note that repeating fitting with the BPASS single-star models was not found to impact the solution) or the evolutionary tracks of red supergiants (e.g., G. A. Vázquez & C. Leitherer 2005). Indeed, visual inspection shows that crucial spectral features for this work, such as the Balmer break strength, are not always in strong agreement across the 10–100 Myr age range in these SSPs.

Observations out to redder wavelengths may help narrow both the age and metallicity estimates. Specifically, observations of the broad photospheric 1.6 μm H$^-$ opacity feature could be leveraged to age-date star clusters in the >10 Myr range owing to red supergiants at early times (J. J. Eldridge et al. 2020) and later red giants and asymptotic giant branch stars (e.g., M. Sawicki 2002). This feature is most apparent at low metallicities (M. Yang et al. 2021) and is broad enough to be identifiable photometrically with JWST MIRI imaging.

The cosmic formation epoch and metallicities of Earendel and 1b are consistent with the age–metallicity sequence observed from GCs in local galaxies (e.g., E. Cezario et al. 2013; C. Usher et al. 2019; see also Figure 4). Furthermore, these findings appear consistent with the ongoing picture of
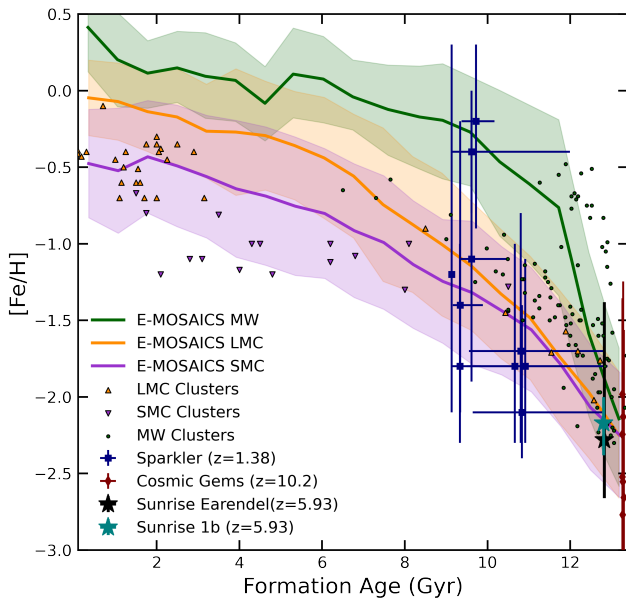
Figure 4. Massive star cluster AMR predicted for MW-, LMC-, and SMC-mass host galaxies predicted by the E-MOSAICS cosmological simulation (J. M. D. Kruijssen et al. 2019; D. Horta et al. 2021) compared to measurements from LMC and SMC clusters (see Table A1 of D. Horta et al. 2021, and references therein) and MW clusters (see Table A1 of J. M. D. Kruijssen et al. 2019, and references therein) from the Sparkler (z = 1.38; A. Adamo et al. 2023), the Cosmic Gems (z ≈ 10.2; A. Adamo et al. 2024), and Earendel and 1b (BPASS results which have the largest uncertainties) from this work. We note that the younger ages of some clusters within both the Sparkler and the Cosmic Gems imply that the best-fit metallicity is dictated in part by enhancement from nebular emission; however, we still approximate $\log(Z/Z_\odot) \approx$ [Fe/H]. All three sets of clusters appear broadly consistent with the predictions of SMC/LMC mass host galaxies, with the Sunrise also showing consistency with an MW-mass host. This figure is adapted from Figure 4 of both A. Adamo et al. (2023) and D. Horta et al. (2021).

star cluster evolution indicated by high-redshift proto-GCs. Earendel and 1b may be evolved cousins of the clusters seen in the z ∼ 10 Cosmic Gems (A. Adamo et al. 2024) and the z ∼ 8.3 Firefly Sparkle (L. Mowla et al. 2024), while perhaps being the precursors to older proto-GCs seen at more intermediate redshifts such as the z ∼ 1.4 Sparkler (L. Mowla et al. 2022; A. Adamo et al. 2023) or the z ∼ 2.5 Relic (K. E. Whitaker et al. 2025).

In Figure 4, we compare the cosmic formation ages and metallicities of various high-redshift clusters to predictions of the cluster age–metallicity relation (AMR) for MW-, LMC-, and SMC-like galaxies presented by D. Horta et al. (2021) from the E-MOSAICS simulation (J. Pfeffer et al. 2018; J. M. D. Kruijssen et al. 2019), where the MW relation is derived from zoom-in simulations in J. M. D. Kruijssen et al. (2019) and the LMC/SMC relations are from D. Horta et al. (2021). While Earendel and 1b show best agreement with SMC/LMC-like halos, the Sunrise galaxy may actually be closer to an MW-like halo mass. E. Vanzella et al. (2023) derive a magnification-corrected total stellar mass $M_\star \sim 10^8 - 10^9\,M_\odot$, which is as much as an order of magnitude higher than the LMC had at this cosmic age (D. R. Weisz et al. 2013). Given the low metallicities inferred for these clusters, it is not immediately clear whether they more closely resemble the in situ or ex situ branch of GCs seen in the MW (D. A. Forbes & T. Bridges 2010). Should Earendel's true metallicity correspond to the lower-age,

higher-metallicity solution seen in Figure 3, this would place it more squarely in the in situ branch, reflecting the rapid buildup of metals achievable in an MW-mass halo (e.g., C. Kobayashi et al. 2020).

4.2. Dust Reddening and Nebular Parameters

Across the three SSP inferences of Earendel and 1b, we find minimal dust reddening $A_V \lesssim 0.1$ mag. The reddening law slope δ is not well constrained; the BPASS and BC03 fits loosely prefer slopes steeper than SMC-like (corresponding to $\delta = 0.45$); however, FSPS generally prefers slopes Calzetti-like ($\delta = 0$) and shallower. The former results may be more consistent with the expectation that high-redshift star-forming galaxies should have steeper reddening laws, for example, the relations of S. Salim et al. (2018) find a slope of $\delta \sim -0.8$ for high-redshift analogs of stellar mass $M_\star/M_\odot \sim 10^8$ similar to the Sunrise (E. Vanzella et al. 2023). By contrast, R. L. Sanders et al. (2024) found the nebular attenuation curve of a high star-forming galaxy at $z = 4.41$ to have an FUV–optical slope similar to J. A. Cardelli et al. (1989), more closely matching the FSPS result. We also do not see a preference for a strong 2175 Å bump, but it is weakly disfavored for all fits to Earendel. Higher SNR is necessary to more confidently rule out the presence of a bump.

None of the fits provide any significant constraints on the ionization parameter or the covering factor, reflecting the preference for evolved cluster ages that have lost the bulk of their ionizing budget. As noted in Section 3, we identify candidate detections of [O III] λ5007 and Hα in the nebular spectrum. Given their low statistical significance, we refrain from making any definitive statements about their nature—the 2D spectrum neither clearly confirms nor denies them to be associated with the underlying arc, and they indeed may merely be a statistical fluke altogether.

The lack of prominent dust reddening and nebular emission is perhaps consistent with the expectation that evolved star clusters are nearly devoid of gas (C. J. Lada & E. A. Lada 2003), as feedback from massive stars is typically expected to expel nearly all of the cluster gas after the first ∼10–20 Myr of the cluster lifetime (F. Calura et al. 2015). While supernovae and Wolf–Rayet stars are expected to provide the bulk of the cluster's dust production within the first ∼10 Myr (R. Schneider & R. Maiolino 2024), it is possible that their dusty ejecta is not efficiently retained within the cluster, or that their overall covering is fairly low.

We note more generally that the use of the S. Salim et al. (2018) reddening law is impactful for capturing uncertainties on the dust and age constraints in this work. Prior work by M. Nakane et al. (2025) has pointed out that, for a fixed D. Calzetti (2001) reddening law, the age, dust, and metallicity affect the continuum in distinct ways, reducing the presence of a degeneracy between these three parameters. However, the dust reddening law of high-redshift galaxies is not necessarily Calzetti-like, nor is it standardized (e.g., R. Fisher et al. 2025), and assuming a fixed slope could induce a bias in the inference or underestimate the uncertainties. Indeed, we find in our fits that the flexible S. Salim et al. (2018) reddening law has a modest but statistically relevant impact on the metallicity compared to implementing a fixed reddening law, even in the regime of $A_V < 0.1$. This is most apparent in the BPASS fit to Earendel shown in Figure 3, where a secondary low-age, high-metallicity solution appears only for steep slopes $\delta < -1$.

Given the broad posterior inferred on the reddening law slope δ in all of our fits, we find that implementing the D. Calzetti (2001) or SMC (K. D. Gordon et al. 2003) reddening laws generally still agrees with our S. Salim et al. (2018) fits to within 1σ; however, in a higher-SNR regime this is likely to no longer be the case. As the dust reddening slope is optimized for in this work, we acknowledge that it does not fully eliminate systematic bias related to the slope; however, we find that it is reduced compared to assuming the fixed slope a priori.

4.3. Is Earendel a Star or Star Cluster?

Prior work by B. Welch et al. (2022a) found that the JWST photometry of Earendel was inconsistent with single-star models from the PoWR and TLUSTY models. Rather, the photometric data are better fit by a binary system, consisting of two massive ($m_{\rm ZAMS} \gtrsim 20\,M_\odot$) stars: an evolved supergiant with $T_{\rm eff,1} \sim 9000\,{\rm K}$, and a main-sequence O star with $T_{\rm eff,2} \sim 34,000\,{\rm K}$. Assuming the largest magnification inferred across all existing lens models for the system, $\mu \sim 17,000$, the total bolometric luminosity for Earendel must reach $L_{\rm bol}/L_\odot \sim 10^6$. B. Welch et al. (2022a) find that the hotter star has a bolometric luminosity $L_{\rm bol}/L_\odot \sim 10^{5.8}$, ~ 0.5 dex greater than the cooler star. Such a system may be somewhat unusual compared to binary systems typically observed in local galaxies, as the hotter, brighter O star would be expected to leave the main sequence prior to its lower-mass companion. Furthermore, the stellar parameters of the cooler star are indicative of passing through the short-lived ($\lesssim 10^4$ yr) yellow supergiant phase (e.g., M. R. Drout et al. 2009); however, the longer-lived ($\sim$Myr) phase of a cool blue supergiant may also match the parameters.

This does not definitively rule out the binary scenario (see A. Nabizadeh et al. 2024 for possible solutions). While it is possible that a single or binary stellar SED fit to the NIRSpec spectrum may provide results more consistent with local observations, it more generally may be difficult to confirm a binary or single-star scenario based on the spectrum alone. The hotter star in the B. Welch et al. (2022a) fit would likely present strong stellar wind features in emission such as the C IV λ1550 or N IV λ1240 P Cygni features given an SMC-like metallicity (undetectable at the PRISM resolution), which would be highly inconsistent with an evolved star cluster. However, if the system is instead metal-poor, the wind mass-loss rate and hence strength of these wind features would be too weak to be detectable in even deep, high-resolution spectra (e.g., C. Leitherer et al. 2014; O. G. Telford et al. 2024). By contrast, the cooler star would present stellar absorption features, such as the Balmer series or Ca II H and K; however, these would also be consistent with an evolved star cluster that consists of many cool stars without strong winds. Ultimately, detection of microlensing-induced photometric variability may be the most promising "smoking gun" indicator (B. Welch et al. 2022b); however, multiepoch imaging has not yet confirmed such variability (B. Welch et al. 2022a).

A star cluster appears to be a natural conclusion from the spectroscopic data and provides an exceptional fit across three different SSP libraries. The physical parameters estimated for the star cluster are consistent with the expectations of a GC progenitor at $z \sim 6$ and are in agreement with the results of simulation work on star cluster formation and evolution. The cluster age is also in alignment with the nondetection of

statistically significant variability across the 2 yr observer-frame baseline (B. Welch et al. 2022a), as such an evolved cluster lacks the massive stars necessary for microlensing to induce large fluctuations (L. Dai et al. 2020).

A third but less well-defined scenario could be that Earendel consists of a "small group" of dozens of stars, requiring a large ($\mu > 1000$) but not extreme ($<10^4$) magnification. Such a group likely cannot be sampled from a standard IMF and must instead be a young system consisting of luminous O and B supergiants in order to reach the necessary bolometric luminosity $L_{\rm bol} \sim 10^7\,L_\odot$ for $\mu \sim \mathcal{O}(10^3)$. Such a system in isolation is not seen in the local Universe, and furthermore it is unclear whether it would match the observed spectrum without significantly fine-tuning the stellar members. However, given the overall small number of stars, microlensing-induced variability should be measurable through precision JWST photometry (L. Dai 2021), and stellar wind features may be detectable in medium-resolution JWST spectroscopy given that the system is not metal-poor.

5. Conclusion

In this Letter, we evaluated two stellar clumps within the $z \approx 5.93$ lensed Sunrise galaxy: Earendel, which we hypothesize is a star cluster, and another star cluster within the galaxy, 1b. The quality of rest-UV through optical JWST NIRSpec spectra of these objects enabled detailed physical parameter estimation of these star clusters. Through SED fitting with three well-tested SSP libraries, BC03, BPASS, and FSPS, we inferred their ages, metallicities, masses, and dust extinctions. We found that both have intermediate ages, $t_{\rm age} \sim 30$–150 Myr, and inferred that their stellar metallicities are $Z \lesssim 10\%\,Z_\odot$, as low as $Z \lesssim 1\%\,Z_\odot$ depending on the SSP model.

The formation ages and metallicities of these clusters are in relative agreement with the AMR of GCs both measured in local galaxies and recovered in simulations. The results are in best agreement with the expectations of SMC/LMC halo mass host galaxies with more marginal consistency with an MW-mass halo, which, given the stellar mass of Sunrise ($M_\star \sim 10^8$–$10^9\,M_\odot$), is likely more appropriate. We have concluded that, when taken together with other high-redshift star cluster measurements, such as the Sparkler or the Cosmic Gems, these clusters appear to corroborate the picture of GC formation and evolution illustrated by local GCs and simulations.

This study represents a first for spectroscopic fitting of evolved star clusters covering from rest-frame UV to optical wavelengths at these redshifts. Past studies have typically relied on nebular emission lines, which is only practical for very young ages, or solely photometry for ascertaining high-redshift star cluster characteristics. While we do not find complete agreement between the three SSP libraries used, we find the low metallicity and intermediate ages inferred to be consistent results. Given that these clusters are extremely faint $m_{\rm F200W} \sim 27$ AB mag, the quality of these measurements showcases the power of JWST and indicates that spectroscopic analyses of evolved star clusters in other high-redshift lensed galaxies are viable.

Appendix A
Tests of Star Formation History

For the SED fitting in this work, we assume that the SFH of these star clusters is representative of an instantaneous burst, which is appropriate for such dense star clusters that likely form their stars over only a few freefall times of the parent giant molecular cloud ($t_{ff} \sim 3$ Myr assuming $R_{GMC} \sim 100$ pc and $\Sigma_{GMC} \sim 1000$ $M_\odot$ pc^{-2}; M. Y. Grudić et al. 2023). However, we also test an exponential decay SFH prescription

in SED fitting on *1b* to evaluate its impact. To conduct this, we use Bagpipes (A. C. Carnall et al. 2018), as the SED fitting approach used in this work only includes the instant burst SFH. Indeed, the age and metallicity binning approach of Bagpipes is likely more suitable for extended SFHs (e.g., not a delta function). We choose our parameter priors to match those described in Section 3, noting that the covering factor is not available in Bagpipes, which effectively assumes a covering factor of unity. We allow τ to freely vary from 1 Myr to 1 Gyr, which lends much greater flexibility to the SED compared to a pure SSP; however, we note that this can permit star formation timescales that may not necessarily reflect observations and simulations.

We find across all three SSPs that the "free τ" inference agrees well with the instantaneous SFH prescriptions, detailed in Table 2. In each, τ converges to less than a few Myr, effectively becoming a "short burst" that closely matches a true SSP. We also explore cases where nebular emission is removed, which returns nearly identical results for BPASS and FSPS; however, the BC03 fit returns a young ($\sim$6 Myr) solution with much higher metallicities $\sim$20% solar. We ultimately disfavor this solution given the lack of detectable nebular emission, whereas nebular emission is readily detected in other young massive clusters within the Sunrise (E. Vanzella et al. 2023). If such a solution is true and this young cluster is somehow void of gas, JWST medium-resolution spectra could reveal stellar wind features, namely the C IV $\lambda1550$ P Cygni feature, which would be strong at that age and metallicity.

Table 2
Free τ SFH SED Parameters

Image	SSP	$\log(t_{age}/\mathrm{yr})$	$\log(\mu M/M_\odot)$	$\log(Z/Z_\odot)$	$\log(\tau/\mathrm{Gyr})$	A_V (mag)	δ	B
Im 1b	BC03	$7.50^{+0.04}_{-0.01}$	$9.19^{+0.02}_{-0.01}$	$-2.10^{+0.06}_{-0.04}$	$-2.56^{+0.18}_{-0.24}$	$0.06^{+0.03}_{-0.02}$	$-1.28^{+0.25}_{-0.24}$	$2.05^{+1.56}_{-0.24}$
	BPASS	$7.69^{+0.05}_{-0.08}$	$9.30^{+0.03}_{-0.04}$	$-2.10^{+0.17}_{-0.12}$	$-2.52^{+0.32}_{-0.29}$	$0.05^{+0.04}_{-0.02}$	$-1.13^{+0.29}_{-0.27}$	$1.77^{+1.60}_{-1.23}$
	FSPS	$8.20^{+0.03}_{-0.05}$	$9.67^{+0.02}_{-0.04}$	$-2.27^{+0.10}_{-0.02}$	$-2.23^{+0.42}_{-0.54}$	$0.03^{+0.05}_{-0.02}$	$0.29^{+0.35}_{-0.58}$	$2.21^{+1.74}_{-1.37}$

Note. Physical parameters for image *1b* using BAGPIPES with the BC03, BPASS, and FSPS SSP libraries and an exponential decay SFH. We list the object, SSP library, population age, magnified stellar mass (μ is the flux magnification factor due to lensing), stellar metallicity, characteristic timescale (τ), visual band extinction, reddening law slope following S. Salim et al. (2018), and reddening law 2175 Å bump strength following S. Salim et al. (2018).

Appendix B
Testing Metallicity Systematics

The precision achieved on the metallicity in each SSP is impressive, at the <0.2 dex level for the higher-SNR $1a$, b. SSP fitting of the rest-UV through optical integrated cluster continuum at this spectral resolution for these intermediate ages is somewhat unexplored, with the majority of works in both the local Universe and at high redshift relying solely on photometry (e.g., A. Wofford et al. 2016) or lacking the rest-FUV. Without the availability of metal-line absorption features, our fitting implies that the continuum alone provides nonnegligible leverage to break well-known age−dust−metallicity degeneracies. We develop three tests to further probe the effectiveness of the continuum for constraining the physical parameters of the stellar population in this intermediate-age, metal-poor regime.

We first use the spectrum of $1b$ and iteratively mask out portions of the spectrum from the FUV to the optical, at each step performing fitting with the BPASS SSP to infer the metallicity (Figure 5; top). Surprisingly, removal of both the FUV and near-UV (NUV; <3800 Å rest frame) is only modestly impactful, softening the metallicity constraints to ~0.5 dex. It is only after further masking beyond the Balmer break to <4800 Å (roughly Sloan Digital Sky Survey g band) that the metallicity constraints are finally eliminated, producing an approximately uniform posterior across a range of metallicities $0.005 \leqslant Z/Z_\odot \lesssim 1$.

We identify that this is due in part to the formation of younger age solutions $\lesssim 10$ Myr with low covering factor $x < 10\%$ that favor all metallicities roughly uniformly. In practice, this could arguably be disfavored a priori by the small covering, which would be surprising for such a young cluster; however, we retain these solutions for the sake of thoroughness. This exercise confirms that the clear Balmer break detected in Earendel and $1b$ is a defining feature in our inference, helping to break age−dust−metallicity degeneracies at these intermediate ages.

We construct a second test to ascertain how the constraints are affected by the noise level (Figure 5, bottom). We create a mock BPASS spectrum of age 50 Myr, metallicity $\log(Z/Z_\odot)=-2.15$, and $A_V=0$ (approximately the $1b$ best fit) without any nebular emission (e.g., $x=0$). We convolve to the PRISM resolution and iteratively implement increasing fractional uniform Gaussian noise scalings from $\sigma_{\rm noise} = 5\%-30\%$ of the model flux. For each noise scaling, we perform fitting using each of the three SSPs and evaluate the inferred metallicity, shown in Figure 5 (bottom). Each model shows general agreement with itself across the different noise levels, and the BC03 and BPASS fits generally agree with the ground-truth BPASS model metallicity. FSPS, however, shows a ~0.8 dex offset toward higher metallicities. This disagreement is not seen in the fits to Earendel or $1b$ and is perhaps somewhat surprising given that both BPASS and FSPS rely on the C3K spectral library in this metallicity regime. Inspection of the posteriors reveals that the FSPS fits converge to a slightly lower ~30 Myr age solution. Extrapolating age–metallicity degeneracy out to older ages could indeed yield lower metallicities; however, these solutions are highly disfavored even in the noisiest models.

Finally, we conduct a third test to evaluate whether the results are a product of a random noise realization. To do so, we once again construct a mock BPASS model as described
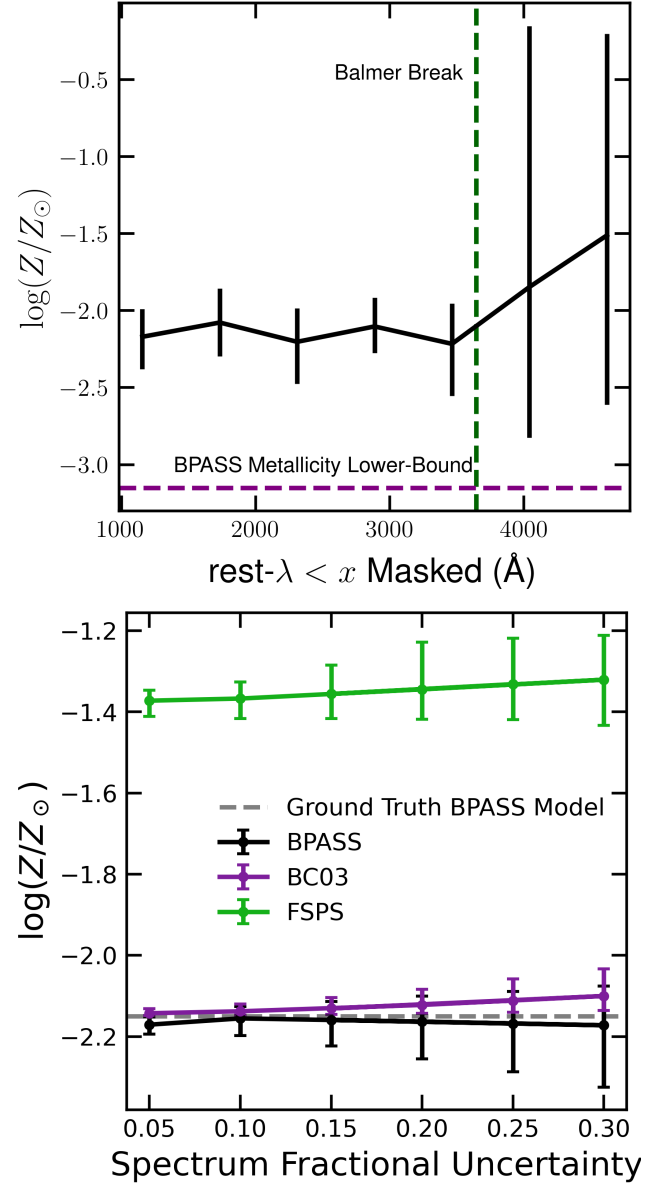

Figure 5. Top: metallicities inferred from the $1b$ NIRSpec PRISM spectrum using the BPASS SSPs (black error bars) with an iterative masking of wavelengths from the rest-FUV to the rest-optical. Masking the FUV through NUV does not appear to significantly affect the inferred metallicity; however, masking beyond the Balmer break (green dashed line), which is clearly detected in the NIRSpec spectrum (Figure 2), results in the metallicity becoming effectively unconstrained. Bottom: metallicities inferred via the BPASS (black), BC03 (purple), and FSPS (green) SSPs from a mock BPASS model of $\log(Z/Z_\odot)=-2.15$, $\log(t_{\rm age}/{\rm yr})=7.7$, and $A_V=0$ with increasing uniform fractional Gaussian noise applied. While BPASS and BC03 recover the ground truth (gray dashed line), FSPS exhibits an offset of ~0.8 dex toward higher metallicities.

above. To apply noise, we take the fractional uncertainties of the $1b$ spectrum, smooth it with a median filter to yield the approximate 1σ noise level, and apply random realizations of Gaussian noise to the mock spectrum following these uncertainties to create 10 mock spectra. We then fit each of these spectra following our SED fitting procedure with the BPASS models to check whether the metallicity is generally well recovered.

As seen in Figure 6, we find that the inferences on these models both generally agree with one another, as well as the
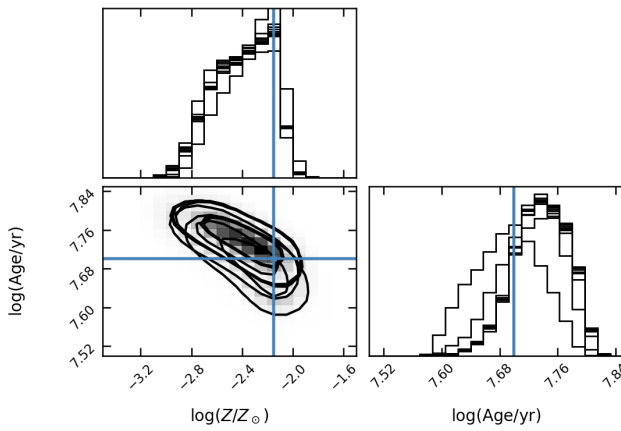
Figure 6. Metallicities and ages posteriors from fitting the BPASS SSPs to 10 mock spectra constructed using a BPASS model of $\log(Z/Z_\odot) = -2.15$, $\log(t_{age}/\mathrm{yr}) = 7.7$, and $A_V = 0$ with noise realizations applied that approximate the wavelength-dependent noise of the $1b$ NIRSpec PRISM spectrum. 2D contours enclose 50% and 90% of the posterior sample. The ground truth (blue lines) is generally recovered to within 1σ; however, the metallicity exhibits a noticeable bias toward lower metallicities.

ground truth to within 1σ. Somewhat concerningly, we do observe a systematic bias toward lower metallicities across all of these fits of $\sim$0.1–0.2 dex. As these do not appear in the prior test that uses uniform fraction noise, this could indicate that this is actually a result of the wavelength-dependent noise in our $1b$ spectrum. It is possible that correlated or wavelength-dependent noise could be biasing the fit, which may also be present in Earendel and $1a$ (in fact, they must, as $1a$ and $1b$ yield similar results in our analysis). However, we find that changing the size of the median filter can change both the strength and direction of the bias, implying that this may instead be a systematic introduced by our noise implementation. Taking this in combination with the magnitude of the biases being comparable to the uncertainties of our inferred metallicities, we conclude that this bias, if real, would have only a modest impact on this work given the current precision of our constraints.

ORCID iDs

Massimo Pascale ⓘ https://orcid.org/0000-0002-2282-8795
Liang Dai ⓘ https://orcid.org/0000-0003-2091-8946
Brenda L. Frye ⓘ https://orcid.org/0000-0003-1625-8009
Aliza G. Beverage ⓘ https://orcid.org/0000-0002-9861-4515

References

Adamo, A., Bradley, L. D., Vanzella, E., et al. 2024, Natur, 632, 513
Adamo, A., Usher, C., Pfeffer, J., & Claeyssens, A. 2023, MNRAS, 525, L6
Asplund, M., Amarsi, A. M., & Grevesse, N. 2021, A&A, 653, A141
Brammer, G. 2022, msaexp: NIRSpec analyis tools, v0.4, Zenodo, doi:10.5281/zenodo.7579050
Bruzual, G., & Charlot, S. 2003, MNRAS, 344, 1000
Calura, F., Few, C. G., Romano, D., & D'Ercole, A. 2015, ApJL, 814, L14
Calzetti, D. 2001, PASP, 113, 1449
Cardelli, J. A., Clayton, G. C., & Mathis, J. S. 1989, ApJ, 345, 245
Carnall, A. C., McLure, R. J., Dunlop, J. S., & Davé, R. 2018, MNRAS, 480, 4379
Carnall, A. C., McLure, R. J., Dunlop, J. S., et al. 2019, MNRAS, 490, 417
Cezario, E., Coelho, P. R. T., Alves-Brito, A., Forbes, D. A., & Brodie, J. P. 2013, A&A, 549, A60
Chen, W., Kelly, P. L., Diego, J. M., et al. 2019, ApJ, 881, 8
Chevallard, J., & Charlot, S. 2016, MNRAS, 462, 1415

Choi, J., Dotter, A., Conroy, C., et al. 2016, ApJ, 823, 102
Coe, D., Salmon, B., Bradač, M., et al. 2019, ApJ, 884, 85
Conroy, C., & Gunn, J. E., 2010 FSPS: Flexible Stellar Population Synthesis, Astrophysics Source Code Library, ascl:1010.043
Dai, L. 2021, MNRAS, 501, 5538
Dai, L., Kaurov, A. A., Sharon, K., et al. 2020, MNRAS, 495, 3192
Dai, L., Venumadhav, T., Kaurov, A. A., & Miralda-Escud, J. 2018, ApJ, 867, 24
de Graaff, A., Brammer, G., Weibel, A., et al. 2025, A&A, 697, A189
de Graaff, A., Rix, H.-W., Carniani, S., et al. 2024, A&A, 684, A87
Dekel, A., Sarkar, K. C., Birnboim, Y., Mandelker, N., & Li, Z. 2023, MNRAS, 523, 3201
Diego, J. M. 2019, A&A, 625, A84
Diego, J. M., Kaiser, N., Broadhurst, T., et al. 2018, ApJ, 857, 25
Diego, J. M., Sun, B., Yan, H., et al. 2023, A&A, 679, A31
Dopita, M. A., Kewley, L. J., Heisler, C. A., & Sutherland, R. S. 2000, ApJ, 542, 224
Drout, M. R., Massey, P., Meynet, G., Tokarz, S., & Caldwell, N. 2009, ApJ, 703, 441
Eldridge, J. J., Beasor, E. R., & Britavskiy, N. 2020, MNRAS, 495, L102
Ferland, G. J., Chatzikos, M., Guzmán, F., et al. 2017, RMxAA, 53, 385
Fisher, R., Bowler, R. A. A., Stefanon, M., et al. 2025, MNRAS, 539, 109
Forbes, D. A., & Bridges, T. 2010, MNRAS, 404, 1203
Frye, B. L., Pascale, M., Pierel, J., et al. 2024, ApJ, 961, 171
Fudamoto, Y., Sun, F., Diego, J. M., et al. 2025, NatAs, 9, 428
Fujimoto, S., Ouchi, M., Kohno, K., et al. 2024, arXiv:2402.18543
Furtak, L. J., Meena, A. K., Zackrisson, E., et al. 2024, MNRAS, 527, L7
Gordon, K. D., Clayton, G. C., Misselt, K. A., Landolt, A. U., & Wolff, M. J. 2003, ApJ, 594, 279
Götberg, Y., de Mink, S. E., Groh, J. H., Leitherer, C., & Norman, C. 2019, A&A, 629, A134
Grudić, M. Y., Hafen, Z., Rodriguez, C. L., et al. 2023, MNRAS, 519, 1366
Grudić, M. Y., Hopkins, P. F., Quataert, E., & Murray, N. 2019, MNRAS, 483, 5548
Heintz, K. E., Watson, D., Brammer, G., et al. 2024, Sci, 384, 890
Hopkins, P. F., Murray, N., Quataert, E., & Thompson, T. A. 2010, MNRAS, 401, L19
Horta, D., Hughes, M. E., Pfeffer, J. L., et al. 2021, MNRAS, 500, 4768
Hosek, M. W., Jr., Lu, J. R., Anderson, J., et al. 2015, ApJ, 813, 27
Ji, L., & Dai, L. 2025, ApJ, 980, 190
Kaurov, A. A., Dai, L., Venumadhav, T., Miralda-Escudé, J., & Frye, B. 2019, ApJ, 880, 58
Kelly, P. L., Diego, J. M., Rodney, S., et al. 2018, NatAs, 2, 334
Kobayashi, C., Karakas, A. I., & Lugaro, M. 2020, ApJ, 900, 179
Kroupa, P. 2001, MNRAS, 322, 231
Kruijssen, J. M. D., Pfeffer, J. L., Crain, R. A., & Bastian, N. 2019, MNRAS, 486, 3134
Krumholz, M. R., McKee, C. F., & Bland-Hawthorn, J. 2019, ARA&A, 57, 227
Lada, C. J., & Lada, E. A. 2003, ARA&A, 41, 57
Lake, W., Grudić, M. Y., Naoz, S., et al. 2025, ApJL, 985, L6
Lange, J. U. 2023, MNRAS, 525, 3181
Leitherer, C., Ekström, S., Meynet, G., et al. 2014, ApJS, 212, 14
Meena, A. K., Zitrin, A., Jiménez-Teja, Y., et al. 2023, ApJL, 944, L6
Menon, S. H., Lancaster, L., Burkhart, B., et al. 2024, ApJL, 967, L28
Messa, M., Vanzella, E., Loiacono, F., et al. 2025, A&A, 694, A59
Mestric, U., Vanzella, E., Upadhyaya, A., et al. 2023, arXiv:2301.04672
Miralda-Escudé, J. 1991, ApJ, 379, 94
Mowla, L., Iyer, K. G., Desprez, G., et al. 2022, ApJL, 937, L35
Mowla, L., Iyer, K., Asada, Y., et al. 2024, arXiv:2402.08696
Nabizadeh, A., Zackrisson, E., Lundqvist, E., et al. 2024, arXiv:2406.12607
Nakane, M., Ouchi, M., Nakajima, K., et al. 2025, arXiv:2503.11457
Oguri, M., Diego, J. M., Kaiser, N., Kelly, P. L., & Broadhurst, T. 2018, PhRvD, 97, 023518
Pascale, M. & Dai, L. 2024, ApJ, 976, 166
Pascale, M., Dai, L., McKee, C. F., & Tsang, B. T. H. 2023, ApJ, 957, 77
Pascale, M., Frye, B. L., Dai, L., et al. 2022, ApJ, 932, 85
Pascale, M., Frye, B. L., Pierel, J. D. R., et al. 2025, ApJ, 979, 13
Pfeffer, J., Kruijssen, J. M. D., Crain, R. A., & Bastian, N. 2018, MNRAS, 475, 4309
Rodney, S. A., Balestra, I., Bradac, M., et al. 2018, NatAs, 2, 324
Salim, S., Boquien, M., & Lee, J. C. 2018, ApJ, 859, 11
Salmon, B., Coe, D., Bradley, L., et al. 2020, ApJ, 889, 189
Sanders, R. L., Shapley, A. E., Topping, M. W., et al. 2024, arXiv:2408.05273
Sawicki, M. 2002, AJ, 124, 3050
Schneider, R., & Maiolino, R. 2024, A&ARv, 32, 2

Scofield, Z. P., Jee, M. J., Cha, S., & Park, H. 2025, arXiv:2504.08879
Stanway, E. R., Eldridge, J. J., & Becker, G. D. 2016, MNRAS, 456, 485
Telford, O. G., Chisholm, J., Sander, A. A. C., et al. 2024, ApJ, 974, 85
Usher, C., Brodie, J. P., Forbes, D. A., et al. 2019, MNRAS, 490, 491
Vanzella, E., Calura, F., Meneghetti, M., et al. 2017, MNRAS, 467, 4304
Vanzella, E., Claeyssens, A., Welch, B., et al. 2023, ApJ, 945, 53
Vázquez, G. A., & Leitherer, C. 2005, ApJ, 621, 695
Venumadhav, T., Dai, L., & Miralda-Escudé, J. 2017, ApJ, 850, 49
Weisenbach, L., Anguita, T., Miralda-Escudé, J., et al. 2024, SSRv, 220, 57

Weisz, D. R., Dolphin, A. E., Skillman, E. D., et al. 2013, MNRAS, 431, 364
Welch, B., Coe, D., Diego, J. M., et al. 2022a, Natur, 603, 815
Welch, B., Coe, D., Zackrisson, E., et al. 2022b, ApJL, 940, L1
Whitaker, K. E., Cutler, S. E., Chandar, R., et al. 2025, arXiv:2501.07627
Williams, C. E., Naoz, S., Lake, W., et al. 2025, arXiv:2502.17561
Williams, L. L. R., Kelly, P. L., Treu, T., et al. 2024, ApJ, 961, 200
Windhorst, R. A., Timmes, F. X., Wyithe, J. S. B., et al. 2018, ApJS, 234, 41
Wofford, A., Charlot, S., Bruzual, G., et al. 2016, MNRAS, 457, 4296
Yang, M., Bonanos, A. Z., Jiang, B., et al. 2021, A&A, 647, A167